





Article

Burn Severity Assessment Using Sentinel-1 SAR in the Southeast Peruvian Amazon, a Case Study of Madre de Dios

Gabriel Alarcon-Aguirre ^{1,2,3} , Reynaldo Fabrizio Miranda Fidhel ¹, Dalmiro Ramos Enciso ⁴, Rembrandt Canahuire-Robles ^{2,3} , Liset Rodriguez-Achata ^{3,5}  and Jorge Garate-Quispe ^{6,*} 

- ¹ Departamento Académico de Ingeniería Forestal y Medio Ambiente, Facultad de Ingeniería, Universidad Nacional Amazónica de Madre de Dios, Puerto Maldonado 17001, Peru; galarcon@unamad.edu.pe (G.A.-A.); rmirandaf@unamad.edu.pe (R.F.M.F.)
 - ² Centro de Teledetección para el Estudio y Gestión de los Recursos Naturales (CETEGERN), Facultad de Ingeniería, Universidad Nacional Amazónica de Madre de Dios, Puerto Maldonado 17001, Peru; rcanahuire@unamad.edu.pe
 - ³ Earth Sciences & Dynamics of Ecology and Landscape Research Group, Universidad Nacional Amazónica de Madre de Dios, Puerto Maldonado 17001, Peru; lrodriguez@unamad.edu.pe
 - ⁴ Departamento Académico de Ingeniería de Sistemas e Informática, Facultad de Ingeniería, Universidad Nacional Amazónica de Madre de Dios, Puerto Maldonado 17001, Peru; eenciso@unamad.edu.pe
 - ⁵ Departamento Académico de Ciencias Básicas, Facultad de Ingeniería, Universidad Nacional Amazónica de Madre de Dios, Puerto Maldonado 17001, Peru
 - ⁶ Department of Evolutionary Biology, Ecology and Environmental Sciences, University of Barcelona, 08028 Barcelona, Spain
- * Correspondence: jgaratqu7@alumnes.ub.edu



Citation: Alarcon-Aguirre, G.; Miranda Fidhel, R.F.; Ramos Enciso, D.; Canahuire-Robles, R.; Rodriguez-Achata, L.; Garate-Quispe, J. Burn Severity Assessment Using Sentinel-1 SAR in the Southeast Peruvian Amazon, a Case Study of Madre de Dios. *Fire* **2022**, *5*, 94. <https://doi.org/10.3390/fire5040094>

Academic Editors: Guilherme Mataveli, Gabriel de Oliveira, Renata Libonati, Liana Anderson and Celso H. L. Silva-Junior

Received: 8 June 2022

Accepted: 6 July 2022

Published: 8 July 2022

Publisher's Note: MDPI stays neutral with regard to jurisdictional claims in published maps and institutional affiliations.



Copyright: © 2022 by the authors. Licensee MDPI, Basel, Switzerland. This article is an open access article distributed under the terms and conditions of the Creative Commons Attribution (CC BY) license (<https://creativecommons.org/licenses/by/4.0/>).

Abstract: Fire is one of the significant drivers of vegetation loss and threat to Amazonian landscapes. It is estimated that fires cause about 30% of deforested areas, so the severity level is an important factor in determining the rate of vegetation recovery. Therefore, the application of remote sensing to detect fires and their severity is fundamental. Radar imagery has an advantage over optical imagery because radar can penetrate clouds, smoke, and rain and can see at night. This research presents algorithms for mapping the severity level of burns based on change detection from Sentinel-1 backscatter data in the southeastern Peruvian Amazon. Absolute, relative, and Radar Forest Degradation Index (RDFI) predictors were used through singular polarization length (dB) patterns (Vertical, Vertical-VV and Horizontal, Horizontal-HH) of vegetation and burned areas. The Composite Burn Index (CBI) determined the algorithms' accuracy. The burn severity ratios used were estimated to be approximately 40% at the high level, 43% at the moderate level, and 17% at the low level. The validation dataset covers 384 locations representing the main areas affected by fires, showing the absolute and relative predictors of cross-polarization ($k = 0.734$) and RDFI ($k = 0.799$) as the most concordant in determining burn severity. Overall, the research determines that Sentinel-1 cross-polarized (VH) data has adequate accuracy for detecting and quantifying burns.

Keywords: Amazon; polarization; absolute and relative predictors; burn ratio; radar forest degradation index

1. Introduction

The consequences of a fire generally include the total or partial loss of vegetation, leaving the soil exposed to erosion, flash flooding, and the release of greenhouse gases into the atmosphere [1–3]. In addition, fire hazards continue after the event, depending on fire severity. Therefore, it is necessary to assess the severity and vulnerability of fire-affected areas for future management [3,4]. In Peru, and specifically in the Amazon region of Madre de Dios, initiatives exist to respond to emergencies in burned areas. The Regional Emergency Operations Center (COER) has the mission to mitigate fire consequences by

quickly assessing the severity of fires and their implications for emergency stabilization and subsequent management. However, its actions are not sufficient to eliminate fire threats.

Currently, the method for determining the severity of burns is through the use of satellite imagery and remote sensing techniques, because they cover large areas and the results are objective [3,5–8]. For this purpose, satellite images from optical sensor have been widely used and have proven to be useful for mapping burned areas [3,6,7,9]. However, there are questions about the detection and quantification of burned areas as mapping products. Likewise, other studies show that the exclusive use of optical data for mapping burned areas is limited by environmental conditions, biophysical characteristics, spectral signature, and cast shadow [8,10]. In emergency situations, such conditions could result in high costs in lives and property damage.

The severity of burns is generally determined by bitemporal indices based on the normalized burn index (NBR) such as the differentiated normalized burn index (dNBR), the relative dNBR (RdNBR), and the relativized burn index (RBR) [6–8]. The related measure, dNBR, refers to the difference between pre- and post-fire datasets. The results of the absolute measure of change in vegetation do not consider the heterogeneity of the landscape, so the burn intensity could vary according to the size and density of vegetation per pixel [5–8,11–13]. Furthermore, these are influenced by vegetation height, moisture content in vegetation and soil, and the exposure of burned material. These characteristics behave adequately for areas not affected or very affected by fire but exhibit lower effectiveness in discriminating intermediate severity levels, where multiple factors interact [6–8,11,14–18].

On the other hand, synthetic aperture radar (SAR), as an active sensor, works nocturnally as well and can be used under almost any weather condition. The potential of SAR technologies in mapping burns through active microwaves presents better detection through cloud cover and less interference from weather conditions. Despite this, studies report that backscattering on vegetation and burned areas depends on polarization (VV, HH, VH, and HV), frequency (X, C, and L), soil moisture, and topography, obtaining precisions lower than the optical ones in many studies [17]. The electric field orientations of the electromagnetic wave are known as polarizations and are usually controlled between Horizontal (H) and Vertical (V) (1. HH; Transmitted-Horizontally and Received-Horizontally, 2. HV; Transmitted-Horizontally and Received-Vertically, 3. VH; Transmitted-Vertically and Received-Horizontally, 4. VV; Transmitted-Vertically and Received-Vertically) in terms of where to incorporate the simultaneous orthogonal polarization component that allows the electric field to be equal to the vector sum of the H and V polarizations based on the phase difference (linearly, elliptically, or circularly) [17]. However, investigations of the interferometric coherence of different bands and polarizations in burned areas indicate a strong relationship of the severity of burning in a stable and dry environment, a situation that is appropriate to the seasonality of burning in the Amazon and needs to be investigated [17,19–22].

In that sense, we use the C-band backscatter data from the Sentinel-1 sensor (with a center frequency of 5.405 GHz and a length of 5.0 cm over a 250 km swath and a high geometric resolution of 5 m by 20 m) to quantify and estimate the severity of burns. For this purpose, we used absolute and relative predictors, as well as the Radar Forest Degradation Index (RDFI) with C-band co-polarization (VV) and cross-polarization (VH), and length patterns (dB) of vegetation and burned areas, validating the accuracy by means of the Composite Burn Index (CBI) calculated from data collected in the field [18–25].

The objective of the study is to estimate the area and severity level of burns through SAR Sentinel-1 in the southeastern Peruvian Amazon. Specifically, we focus on forests during 2020 in the district of Tahuamanu, Madre de Dios. The specific objectives of the study were: (a) to quantify the area of burns, and (b) to estimate the severity levels of burns. The hypothesis of the study indicates that the area and severity level of burns using SAR Sentinel-1 images can be determined through processing techniques employing the absolute/relative predictors (VH) and RDFI, with a kappa accuracy greater than 0.70.

2. Materials and Methods

2.1. Study Area

The study area comprises the district of Tahuamanu in the department of Madre de Dios, in the southeastern Peruvian Amazon. The district of Tahuamanu encompasses a total area of 15,079 km² (Figure 1) and includes agricultural areas, timber, and non-timber forest concessions, as well as indigenous lands [26]. It is located between parallels 9°51'12" and 11°55'56" south latitude and meridians 68°59'18" and 72° 14'39" west longitude, with an altitude between 200 m and 550 m above sea level [27–31].

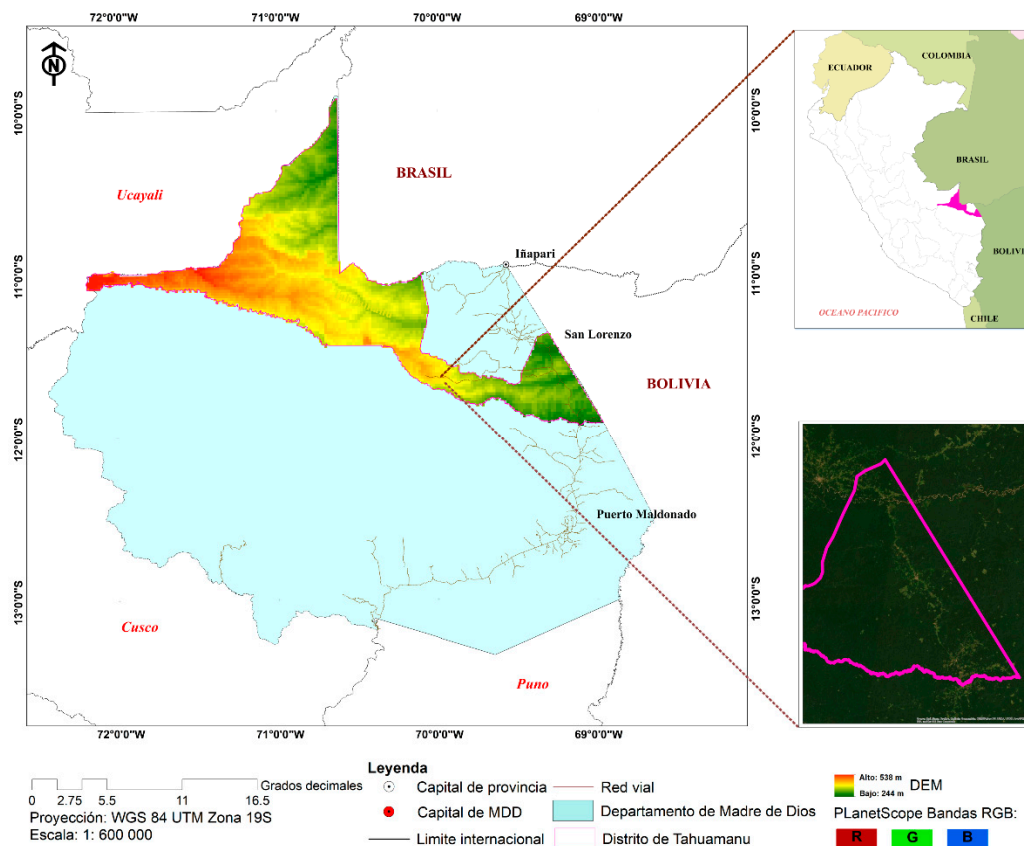


Figure 1. Location of the study area, Distrito de Tahuamanu, Madre de Dios—Perú.

The study area is in the tropical rainforest. The average annual temperature is 25 °C, with maximum temperatures reaching 38 °C, and minimum temperatures dropping to 8 °C. The coldest months are December, January, and February, while the warmest months are June, July, and August [32,33]. A climatic phenomenon characterized by low temperatures, due to cold air masses arriving from the American Southeast, is known locally as “friaaje” or “surazo” [34–36]. The average annual relative humidity varies from 70% to 85% [35,36].

2.2. Description and Data Processing

2.2.1. SAR Sentinel-1 (S1)

The European Space Agency (ESA), through the Sentinel-1 mission, provides world-wide coverage of freely available dual or cross-polarized C-band SAR images (with Ground Range Detected scenes) at a time interval of 6 days and from 1 to 3 days revisit rate, depending on the orbits (ascending and descending) of the satellites (1A and 1B) and the overlap (Table S2). All SAR images used in this study were acquired in Interferometric Wide (IW) mode, VV polarization (Figure S2), VH (Figure S3), and descending orbit (Tables S1 and S2).

The type of study applied was correlational and predictive, with a transactional (cross-sectional) design [37]. Sentinel-1 data were accessed through the Google Earth Engine

(GEE) portal. Using the GEE processing engine, the complex data were converted into radiometric and geo-coded terrain data, obtaining the co-registration of the scenes and sensor track. Representative pixel corrections were performed, and speckle noise was reduced. For this, spatial temporal weighting was performed, and speckle reduction filters were applied to the detected image, while the multi-look reduced speckle at the cost of resolution [3,38]. Geometric correction (geocoding) was performed to correct for the satellite sensor's topographical variations and tilt. The available algorithm, Range Doppler Terrain Correction Operator, uses the digital elevation model (DEM) of the Shuttle Radar Topography Mission (SRTM) for each pre-and post-scenario [3,38].

The mean backscatter values were initially evaluated before being spatially located in the study area (before and after the fire) [3]. The analysis applied absolute, relative, and RBR predictor equations by RDFI (Equations (1)–(9)) from the VV and VH backscatter data [3,18,39] to quantify the area and severity of burnings:

$$\text{Abs_VV} = \text{VV}_{\text{pre}} - \text{VV}_{\text{post}} \quad (1)$$

$$\text{Abs_VH} = \text{VH}_{\text{pre}} - \text{VH}_{\text{post}} \quad (2)$$

$$\text{Rel_VV_1} = \frac{\text{VV}_{\text{pre}} - \text{VV}_{\text{post}}}{\text{VV}_{\text{pre}}} \quad (3)$$

$$\text{Rel_VH_1} = \frac{\text{VH}_{\text{pre}} - \text{VH}_{\text{post}}}{\text{VH}_{\text{pre}}} \quad (4)$$

$$\text{Rel_VV_2} = \frac{\text{VV}_{\text{pre}} - \text{VV}_{\text{post}}}{\sqrt{\text{VV}_{\text{pre}}}} \quad (5)$$

$$\text{Rel_VH_2} = \frac{\text{VH}_{\text{pre}} - \text{VH}_{\text{post}}}{\sqrt{\text{VH}_{\text{pre}}}} \quad (6)$$

$$\sigma_{0,\text{dB}} = 10 \times \log_{10} \times \sigma_0 \quad (7)$$

where VV and VH represent the backscatter coefficients in unit σ_0 (Sigma0) to be expressed in decibels (dB).

The RBR involved the calculation of the post-fire ratio of backscatter coefficients in units of power (Equation (8)):

$$\text{RBR}_{xy} = \frac{\text{Postfireaveragebackscatter}_{xy}}{\text{Prefireaveragebackscatter}_{xy}} \quad (8)$$

where xy is an individual polarization or radar index.

RBR was developed for each polarization (VV and VH) and for RDFI (Equation (9)), which shows the strength of the double bounce and backscatter of the soil directly.

$$\text{RDFI} = \frac{(\text{VV} - \text{VH})}{(\text{VV} + \text{VH})} \quad (9)$$

where VV and VH represent the backscatter coefficient in power units.

Equations (1) and (2) measure the absolute changes in the landscape after the fires, while Equations (3)–(6) show the relative changes with respect to the initial condition of the soil before the fire [3,18,39].

The absolute and relative parameters for measuring the severity level of burns (Abs_VV, Abs_VH, Rel_VV1, Rel_VV_2, Rel_VH_1, and Rel_VH_2) used the criteria shown in Table 1 [3,18,39].

Table 1. Decision criteria for developing the SAR Sentinel-1 burn severity model using absolute and relative values ¹.

Decision Criteria	Severity of Burns
Rel_VV/VH $1 \leq 0.57$; Evergreen = No; Abs_VV/VH ≤ 0.03	Moderate
Rel_VV/VH $1 \leq 0.57$; Evergreen = No; Abs_VV/VH > 0.03	High
Rel_VV/VH $1 \leq 0.57$; Evergreen = Yes; Abs_VV/VH ≤ 0.03	Low
Rel_VV/VH $1 \leq 0.57$; Evergreen = Yes; Abs_VV/VH > 0.03	Moderate
Rel_VH $1 > 0.57$; Abs_VV/VH ≤ 0.19	High
Rel_VV/VH $1 \leq 0.57$; Abs_VV/VH > 0.19	Moderate

¹ Adapted from Addison and Oommen [3].

On the other hand, to measure RBR by means of the RDFI from the backscatter data VV and VH [3,18,39], the criteria shown in Table 2 were used.

Table 2. Decision criteria for developing the SAR Sentinel-1 burn severity model using RDFI ¹.

Decision Criteria	Severity of Burns
RDFI = -0.6 to -0.47	Low
RDFI = -0.47 to 0.04	Moderate
RDFI ≥ 0.04	High

¹ Adapted from Tanase et al. [17] and Tanase et al. [18].

The final results were applied to post-classification by the majority/minority analysis method with a kernel size of 3×3 to rectify and reclassify each image pixel by pixel [29,40,41]. The processing used SNAP ESA, GEE, ArcGis Pro 2.1[®], and ArcGis 10.5[®] provided by the Centro de Teledetección para el Estudio y Gestión de los Recursos Naturales (CETEGERN) of the Universidad Nacional Amazónica de Madre de Dios [29] and the Center for Amazonian Scientific Innovation (CINCIA).

2.2.2. Accuracy Assessment and Field Data

A surface area of 15,079 km² was established for the field data collection, in 384 field samples, selected using a stratified random sampling method and inclusion and exclusion techniques (Figure S1) [42–44]. The sampled plots in the field had a minimum size of 30 m \times 30 m and were distributed in a representative manner [44] among burn severity categories: low (n = 128), moderate (n = 128), and high (n = 128) (Figures 2 and S1).

Data were analyzed using statistical procedures. We applied tests for the evaluation of the predictive power of the absolute, relative, and index values with the actual field information (CBI) and employed the confusion matrix and the kappa coefficient (κ) [3,29,43,45–48].

The continuous in-class CBI proposed by Key and Benson [49], adapted and modified for the study, was used in the field to measure fire severity among the following categories: no change (CBI = 0), low severity ($0 < \text{CBI} \leq 1$), medium severity ($1 < \text{CBI} \leq 2$), and high severity (CBI > 2) (Table 3).

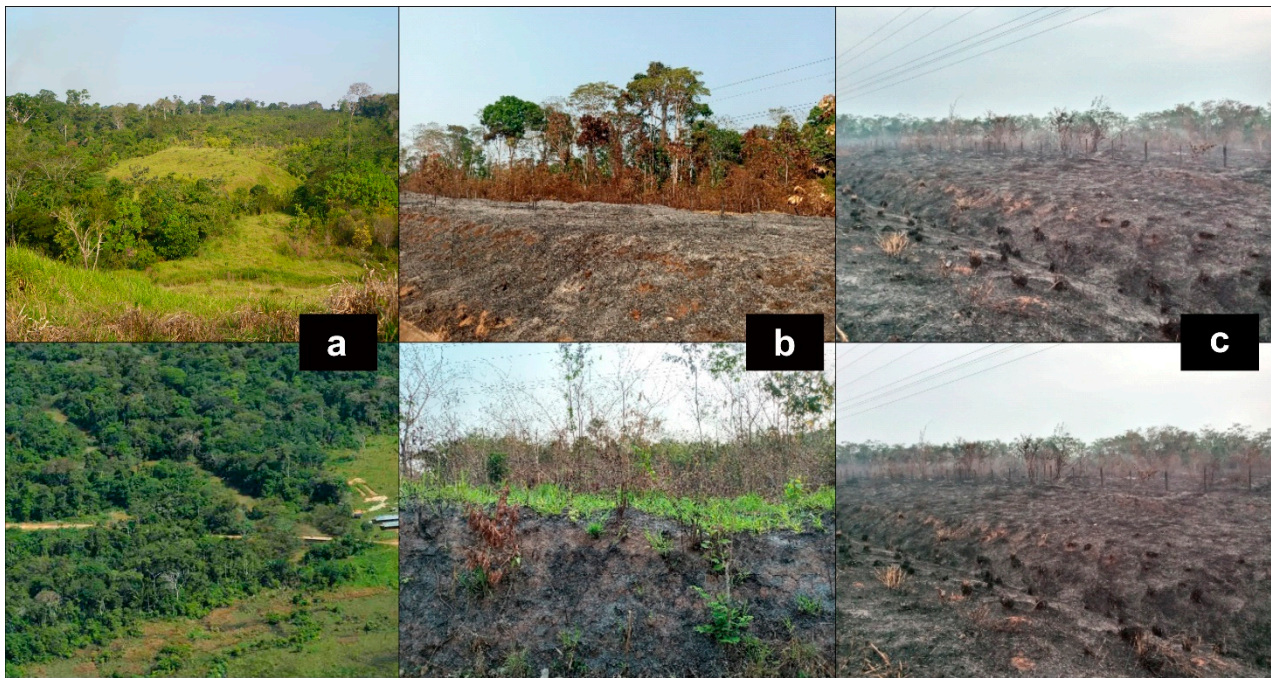


Figure 2. Types of burn severity (CBI): low severity (a), moderate severity (b), and high severity (c).

Table 3. Definitions of CBI severity categories for comparing absolute, relative values, and RBR by RDFI from VV and VH backscatter data ¹.

Category	CBI	Description
Unburned	0	The location did not experience any fires. This may also include a location that recovers quickly after fires.
Low	>0 to ≤ 1	Minimal vegetation consumption: vegetation fragments affected.
Moderate	1 to ≤ 2	The landscape exhibits transitional conditions between the low and high severity characteristics described above.
High	>2	Approximately 90% to total vegetation consumption. Sites typically exhibit greater than 50% mineral soil cover or freshly exposed rock fragments.

¹ Adapted from Key and Benson [49].

From the results of the statistical analysis, we determined the overall accuracy and Cohen's Kappa Index (Equations (10) and (11)), which measures the overall performance of the model [48] and inter-observer concordance [29,50,51] in the correct identification of the three burn severity classes.

$$\text{Overall accuracy} = \frac{TP}{TP + FP + TN + FN} \quad (10)$$

where TP is true positive, TN is true negative, FP is false positive, and FN is false negative.

$$\text{Kappa}(k) = \frac{f_0 - f_c}{1 - f_c} \quad (11)$$

where f_0 is the proportion of matching units, and f_c is the proportion of units expected to match at random.

3. Results

3.1. Estimation of Burned Areas Using the Sentinel-1 (S1) Sensor

To evaluate SAR burn severity according to local topography, the Composite Burn Index (CBI) was used as a function of sensor type and orbit direction (S1A downward) (Table

S1 and Figures 3 and 4). The reduction of weather effects was achieved through the acquisition of SAR images with VV and VH polarization in environmental conditions of minimum humidity pre- (16 and 21 May 2020) and post-fire (1 and 6 October 2020) (Table S2). For the Tahuamanu district, Abs_VVV, Abs_VH, Rel_VV_1, Rel_VH_1, Rel_VV_2, Rel_VH_2, RBRxy, and RDFI (Equations (1)–(10)) were posed as quotients. The C-band backscatter data from the Sentinel-1 sensor with a center frequency of 5.405 GHz and a length of 5 cm over a 250 km swath and a high geometric resolution of 5 m by 20 m are useful for mapping burn severity [3,17,18].

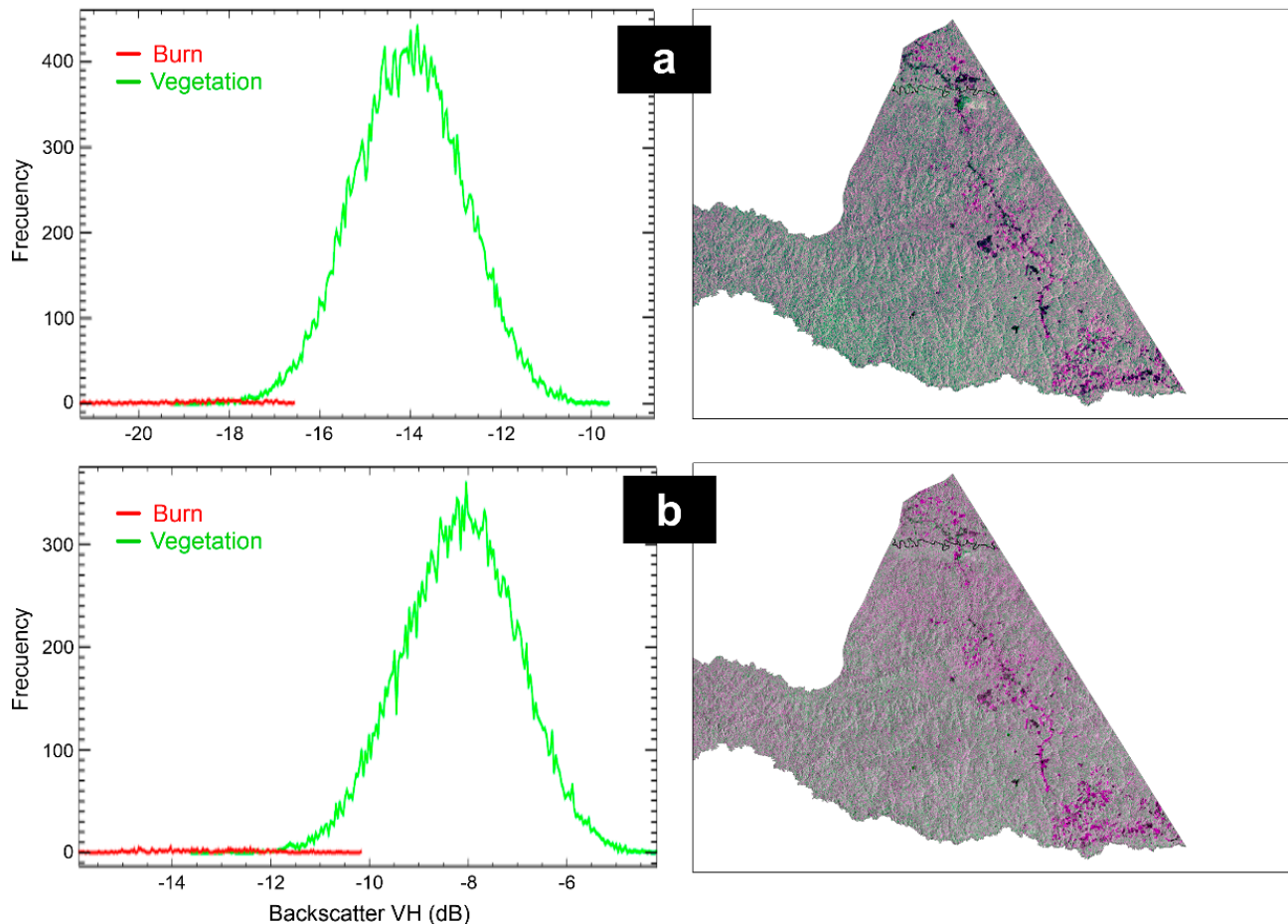


Figure 3. Wavelength (dB microwave) backscatter VV (a) and VH (b) for vegetation and burned areas.

C-band co-polarization (VV) and cross-polarization (VH) coherence were used to measure the sensitivity of volume changes and the combustion of biomass (leaves and branches) and consequently the damaged, thin, and dry vegetation resulting from the burn generating less backscatter (Figures 3 and 4) [3]. Figures 3 and 4 show the spatial patterns in decibels (dB) and indices of the vegetation and burned areas, such as the severity of the burn (CBI), where the dark areas show the differential increase in polarization and the greater influence of the surface properties of the burned area.

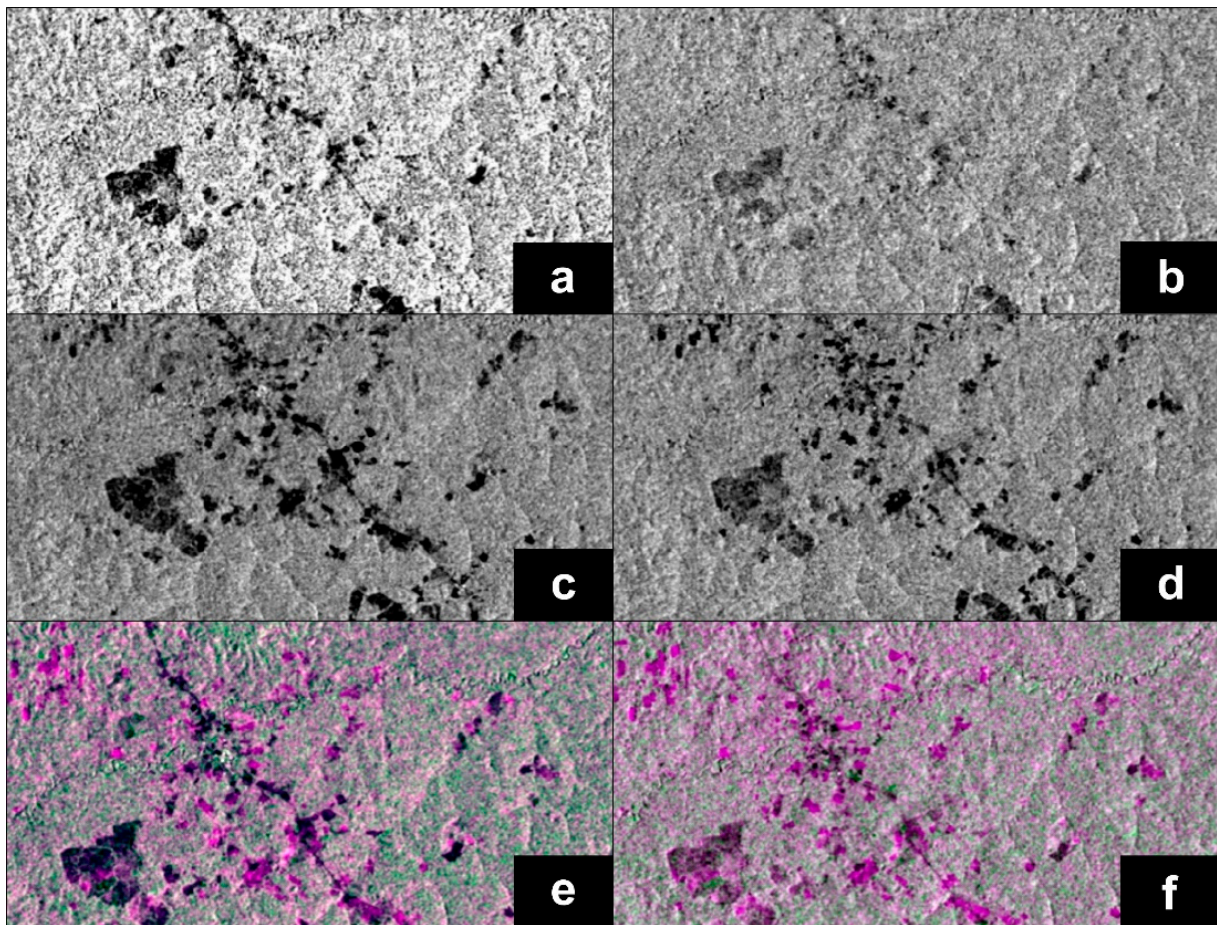


Figure 4. Sentinel-1 C-band VV co-polarization (a,b), VH cross-polarization (c,d), and pre- and post-burn composite (e,f).

3.1.1. Burn Quantification

The data shown in Figure 5 were characterized by the greatest difference in backscatter between burned and unburned vegetation. The SAR Sentinel-1 VV and VH polarization images were acquired under two climatic conditions: (1) late rainy season, and (2) high temperature (Table S1). The co-polarized backscatter coefficient VV increased minimally with burn severity with respect to the C-band VH polarization (Figure 3). This minimal variation of the backscattering of the burned areas of VV over VH could be explained with the decrease of the canopy and consequently the exposure of residual vegetation and soil [17,18,39,52]. In that sense, the most intense and darkest zones (black and purple) show the differential increase in polarization and the greatest influence of the surface properties of the burned area (Figures 4 and 5).

The burns of the mapped vegetation in the forests of the district of Tahuamanu with SAR Sentinel-1 images used absolute, relative, and RBR predictors by means of RDFI quantified areas of 2963 ha (Ab_Rel_VV_1), 3108 ha (Ab_Rel_VV_2), 2920 ha (Ab_Rel_VH_1), 3972 ha (Ab_Rel_VH_2), and 3496 ha (RDFI_VVH), respectively (Figures 6 and S4–S8). These results showed differences in the spatial distribution and surface area of burned areas, ranging from 1052 ha between the minimum (Ab_Rel_VH_1) and maximum (Ab_Rel_VH_2).

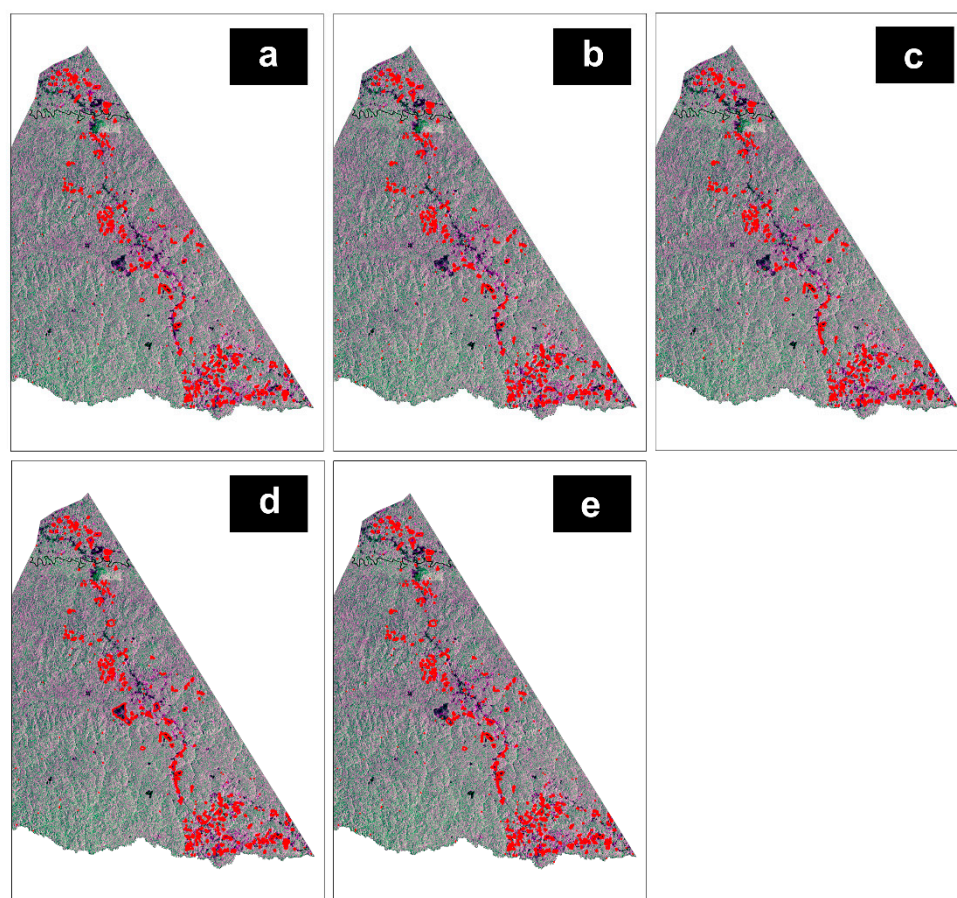


Figure 5. Sentinel-1 C-band burn quantification using absolute and relative values of VV, VH, and pre- and post-burn 2020 backscatter data: (a) relative absolute VV_1, (b) relative absolute VV_2, (c) relative absolute VH_1, (d) relative absolute VH_2, (e) RDFI VVVH.

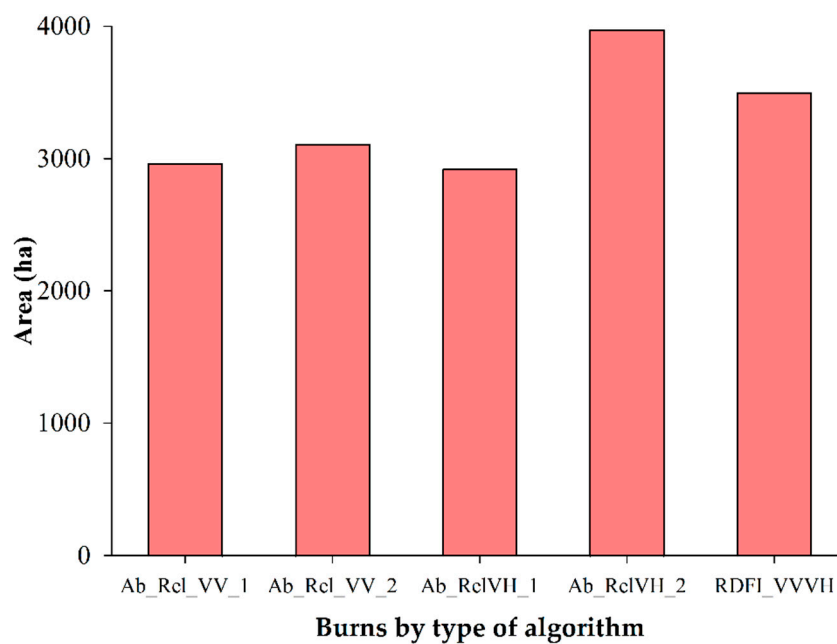


Figure 6. Quantification of burned areas by absolute and relative values, and RBR by RDFI of pre- and post-fire 2020 VV and VH backscatter data; Equations (1)–(9).

3.1.2. Burn Severity

To determine burn severity, Sentinel-1 SAR backscatter was used by means of absolute and relative predictors and RBR by means of RDFI according to the parameters proposed in Tables 1–3. The results showed a strong association between backscatter and burn severity with co-polarization (VV) and cross-polarization (VH). Absolute/relative coefficient crossover and RDFI were used to determine and discriminate the relative strength of polarization and burn severity. The simultaneous use of co-polarized channels and cross-polarization allowed for the determination of the highest coefficients and the lowest errors for the C-band. The highest records in the C-band in units of decibels (dB) were related to the level of vegetation burn severity.

Absolute and relative values of co-polarization and cross-polarization indices showed Abs_VV values from -18.71 to -0.03 (moderate/low), 0.03 to 0.19 (high), and >0.19 (moderate); Abs_VH values <0.05 (moderate/low), from 0.05 to 0.09 (high/moderate), and from 0.09 to 0.16 (high); Rel_VV_1 values from -18.3 to 0.57 (moderate/high) and >0.57 (high); Rel_VH1 with values from 0.76 to 2.92 (high); Rel_VH_2 from 0.41 to 0.57 (moderate) and from 0.57 to 1.52 (high); and Rel_VH_2 from -18.37 to 0.57 (high/moderate/low), and >0.57 (high) (Figure 7).

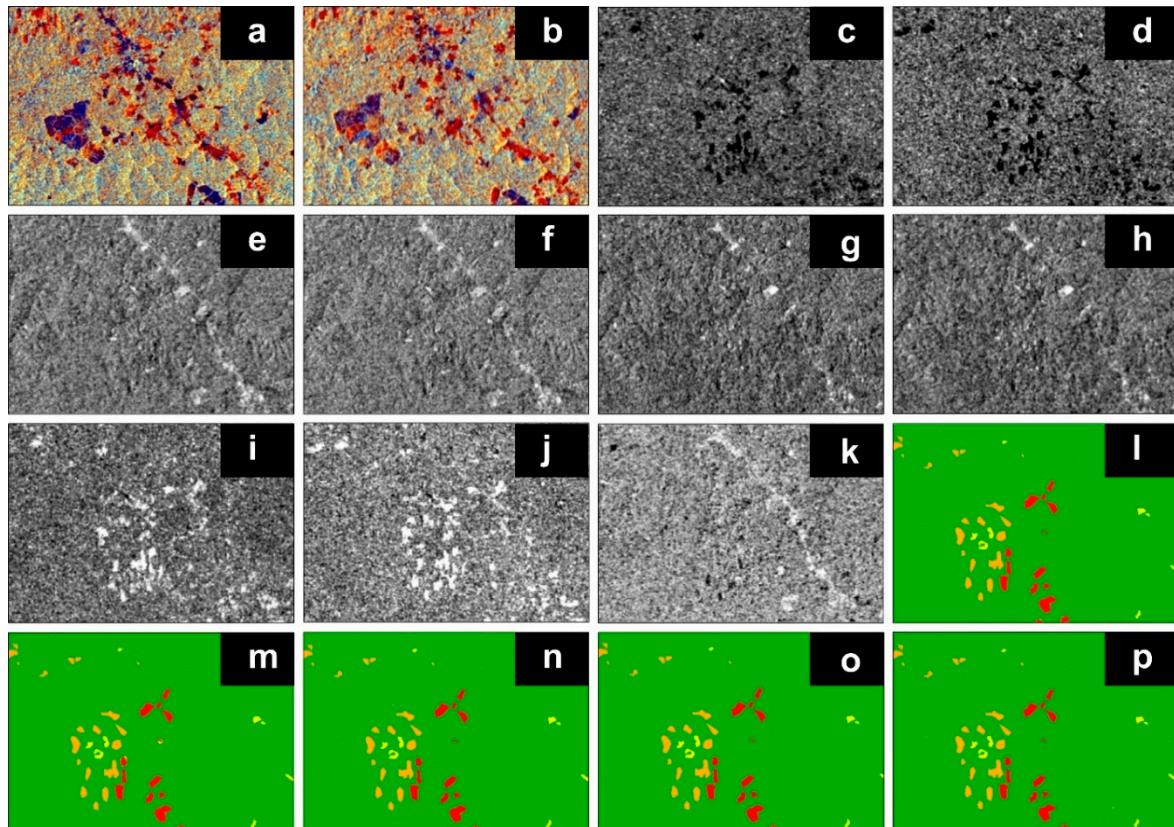


Figure 7. Sentinel-1 C-band, burn severity using absolute and relative values of backscatter data VV, VH, and pre- and post-burn 2020: (a) pre-burn, (b) post-burn, (c) absolute VV, (d) absolute VH, (e) relative VV, (f) relative VH, (g) relative absolute VV_1, (h) relative absolute VV_2, (i) relative absolute VH_1, (j) relative absolute VH_2, (k) RDFI VVVH, (l) relative absolute burn severity VV_1, (m) relative absolute burn severity VV_2, (n) relative absolute burn severity VH_1, (o) relative absolute burn severity VH_2, and (p) RDFI burn severity VVVH.

In the case of burned areas based on RBR with RDFI, the severity of burns was quantified with values of indices from -0.6 to -0.47 at the low level, from -0.47 to 0.04 at the moderate level, and from 0.04 to 0.16 at the high level (Figure 8).

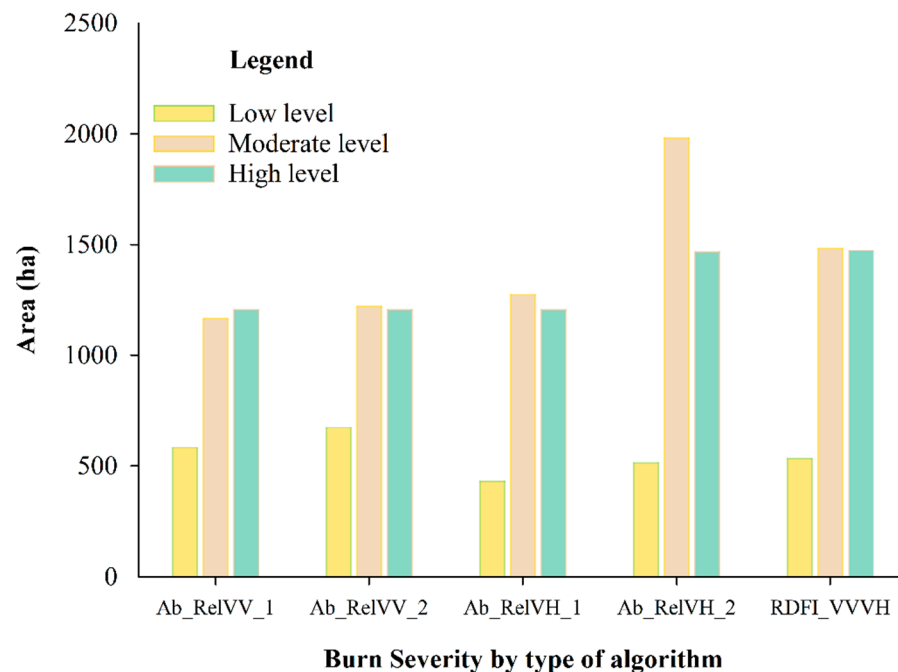


Figure 8. Areas by burn severity level using absolute and relative values and Burn Ratio (RBR) by Radar Forest Degradation Index (RDFI) from pre- and post-fire 2020 VV and VH backscatter data.

From the data, it was possible to detect and quantify the severity of the burns in the images: (1) Ab_Rel_VV_1 with 586 ha (low), 1167 ha (moderate), and 1209 ha (high); (2) Ab_Rel_VV_2 with 676 ha (low), 1223 ha (moderate), and 1208 ha (high); (3) Ab_Rel_VH_1 with 435 ha (low), 1277 ha (moderate), and 1208 ha (high); (4) Ab_Rel_VH_2 with 519 ha (low), 1983 ha (moderate), and 1470 ha (high), and; (5) RDFI_VVVH with 536 ha (low), 1484 ha (moderate), and 1475 ha (high) (Figures 8 and S9–S13).

3.2. Accuracy Assessment

To measure the accuracy of burn severity at different co-polarization and cross-polarization ratios, a coefficient of agreement analysis was carried out for nominal scales (kappa), and a global accuracy matrix using field data on plot burn severity (CBI) [1,5,12,44,51,53]. The proportion of plots ($n = 384$) with CBI values (Table 4) was relatively significant. However, more detailed measurements of vegetation structure parameters are needed to increase the significance of the statistical analysis [17,18,39,51,54–56].

The SAR Sentinel-1 backscatter data detected $k = 0.523$ for VV_1, $k = 0.516$ for VV_2, $k = 0.477$ for VH_1, $k = 0.672$ for VH_2, and $k = 0.742$ for VVVH, where more than half of the joint judgments were in agreement (excluding chance). The marginals were such that k_M was 1.004 (VV_1), k_M was 1.016 (VV_2), k_M was 1.012 (VH_1), k_M was 1.043 (VH_2), and k_M was 1.051 (VVVH), so a substantial part of the disagreement was a consequence of marginal discrepancies (where k_M is the maximum value of k). The probable population value (at 95%) of x for VV_1 was estimated to be between 0.454 and 0.593, for VV_2 between 0.445 and 0.586, for VH_1 between 0.405 and 0.548, for VH_2 between 0.610 and 0.734, and of VVVH between 0.686 and 0.799, with moderate concordance strengths (0.41–0.60) for VV_1, VV_2, and VH_1, while for VH_2 and VVVH there was a considerable concordance strength (0.61–0.80) [51]. At the overall precision level, they reported values of 0.682, 0.677, 0.651, 0.781, and 0.828, respectively. The z -values for VV_1 (14.506), VV_2 (14.289), VH_1 (13.207), VH_2 (18.602), and VVVH (20.568) measured the difference between an observed statistic and its hypothetical population parameter in standard deviation units, being significant at a probability of ($p < 0.001$) (Table 4).

Table 4. Confusion matrix and kappa index of CBI test data (columns) versus SAR Sentinel-1 data of absolute and relative values of VV and VH backscatter data of 2020 burns. (a) Relative absolute burn severity VV_1; (b) relative absolute burn severity VV_2; (c) relative absolute burn severity VH_1; (d) relative absolute burn severity VH_2, and (e) RDFI burn severity VVVH.

Category (a)		CBI				Category (b)		CBI			
		Low	Moderate	High	$f_{SAR\ Sentinel-1}$			Low	Moderate	High	$f_{SAR\ Sentinel-1}$
SAR Sentinel-1 (VV_1)	Low	88 (42)	23	15	126	SAR Sentinel-1 (VV_2)	Low	86 (41)	23	15	124
	Moderate	24	83 (43)	22	129		Moderate	23	85 (44)	24	132
	High	16	22	91 (43)	129		High	19	20	89 (43)	128
	f_{CBI}	128	128	128	384		f_{CBI}	128	128	128	384
$f_o=$	262		$f_c=$	128		$f_o=$	260		$f_c=$	128	
$k=$	0.523		$k_M=$	1.004		$k=$	0.516		$k_M=$	1.016	
$\sigma_k=$	0.0356		$\sigma_{k_o}=$	0.0361		$\sigma_k=$	0.0358		$\sigma_{k_o}=$	0.0361	
$z=$	14.506		Confusion matrix=	0.682		$z=$	14.289		Confusion matrix=	0.677	
Category (c)		CBI				Category (d)		CBI			
		Low	Moderate	High	$f_{SAR\ Sentinel-1}$			Low	Moderate	High	$f_{SAR\ Sentinel-1}$
SAR Sentinel-1 (VH_1)	Low	79 (41)	25	19	123	SAR Sentinel-1 (VH_2)	Low	101 (43)	15	13	129
	Moderate	27	83 (44)	21	131		Moderate	15	104 (46)	20	139
	High	22	20	88 (43)	130		High	12	9	95 (39)	116
	f_{CBI}	128	128	128	384		f_{CBI}	128	128	128	384
$f_o=$	250		$f_c=$	128		$f_o=$	300		$f_c=$	128	
$k=$	0.477		$k_M=$	1.012		$k=$	0.672		$k_M=$	1.043	
$\sigma_k=$	0.0365		$\sigma_{k_o}=$	0.0361		$\sigma_k=$	0.0316		$\sigma_{k_o}=$	0.0361	
$z=$	13.207		Confusion matrix=	0.651		$z=$	18.602		Confusion matrix=	0.781	
Category (e)		CBI				Category (f)		CBI			
		Low	Moderate	High	$f_{SAR\ Sentinel-1}$			Low	Moderate	High	$f_{SAR\ Sentinel-1}$
SAR Sentinel-1 (VVVH)	Low	108 (44)	11	12	131	SAR Sentinel-1 (VVVH)	Low	108 (44)	11	12	131
	Moderate	13	111 (47)	17	141		Moderate	13	111 (47)	17	141
	High	7	6	99 (37)	112		High	7	6	99 (37)	112
	f_{CBI}	128	128	128	384		f_{CBI}	128	128	128	384
$f_o=$	318		$f_c=$	128		$f_o=$	318		$f_c=$	128	
$k=$	0.742		$k_M=$	1.051		$k=$	0.742		$k_M=$	1.051	
$\sigma_k=$	0.0289		$\sigma_{k_o}=$	0.0361		$\sigma_k=$	0.0289		$\sigma_{k_o}=$	0.0361	
$z=$	20.568		Confusion matrix=	0.828		$z=$	20.568		Confusion matrix=	0.828	

The reliability results determined the cross ratios of absolute and relative cross-polarization values VH_2 ($k = 0.734$) and the RBR by RDFI ($k = 0.799$) to be the most concordant to determine the severity of burns, showing considerable concordance strength with respect to the moderate strength of the other ratios [1,5,12,44,51,53].

4. Discussion

Historically, burn-related forest disturbances in the Amazon have been associated primarily with the conversion of natural forests to agricultural uses [28,30,57,58]. Various attempts to establish policies and management instruments have existed to regulate burning, but they have not worked due to the weak presence of the government in rural areas [31,59].

An advantage, but not a determining factor, is the occupation of areas with forest titles, titled agricultural lands, or indigenous communities, which guarantee some security and protection against encroachment but are not free from burning. Despite all this, there is evidence of invasions for agricultural purposes, where slash-and-burn activities are carried out. In most cases, uncontrolled burning extends to agricultural fields, pastures, pastureland, grasslands, secondary forests, and primary forests [22,60–63].

Another common situation in the study area is patch and edge burning. Most burns are provoked by small and medium farmers by (1) slash and burn forestry, and (2) uncontrolled logging, in which trees are affected by fire and then they are logged, even though these forests are able to recover after forest fires [20,22,64,65].

Many studies show the potential of using radar and combined radar and optical sensors to detect vegetation disturbance from burning [17,18,22,52,60,66,67]. We used Sentinel-1 SAR with VV and VH polarizations to achieve a higher observation density and to overcome the influence of environmental factors on the optical time series. The results show that the vertical and horizontal sensitivities of SAR to changes in photosynthetic and non-photosynthetic vegetation cover go beyond a binary detection (forest and burns); therefore, its use can be very broad [3,22,39,52,55]. In this context, studies of burn patterns identified in Amazonian regions such as Pando (Bolivia) and Acre (Brazil) are similar to those in the Madre de Dios region [21,27,68].

The Sentinel-1 C-band SAR data with VV and VH backscatter were acquired under two climatic conditions: (1) end of the rainy season, and (2) high temperature (Table S1). The backscattering coefficient VV increased minimally with burn severity with respect to VH polarization. This increase in the backscattering of burned areas is supported by the reduced presence of canopy and exposure of residual vegetation and soil. Consequently, the penetration of vertical waves generates a lower response. However, the dispersion and spatial quantification of burn severity may vary in their behavior and present a better level of detection with vertical and horizontal backscattering [17–19,39,52,54,55,67].

Areas not affected by burns showed 0 dB of change, with values around 1. Crossing absolute and relative values of the cross-polarization VH, the coefficient Ab_Rel_VH_1 detected a slight underestimation in the quantification of burn severity relative to the other ratios, as opposed to the predictor Ab_Rel_VH_2, where it exhibited a slight overestimation with respect to the others. While the RDFI_VVVH showed much more consistent results, this could be due to the dispersion of the use of co-polarization (VV) and cross-polarization (VH) in the same quotient (Figure 7, Figures S8 and S13) [17,18,25,60,69], as well as the wide opening of the vertical and horizontal waves in the detection of burns due to the reduction of the canopy and, as a consequence, the exposure of residual vegetation and soil [17–19,39,52,54,55,67].

The proportion of burn severity in the ratios used showed average ranges from 38% to 42% at the high level, from 39% to 50% at the moderate level, and from 13% to 22% at the low level. On the other hand, the increase in fire severity in Ab_Rel_VV_1, Ab_Rel_VV_2, Ab_Rel_VH_1, Ab_Rel_VH_2, and RDFI_VVVH corresponds to the increase in post-burn values. The highest values are due to a differentiated effect of the severity of the burns and are recorded in the VV and VH polarizations, with VV backscattering

showing a decrease due to the effect of the elimination of scattering elements, compensated by an increase in surface scattering [3,63,69,70]. The burn ratios varied from unburned to high severity levels, and the findings resemble those reported by other researchers, in which the values were elevated by the presence of dispersant elements in Amazonian forests [3,5,21,22,61–63,66,69–71]. However, the behavior is the opposite in coniferous, temperate, or boreal forests [17–19,24,72,73].

Regarding the accuracy of burn severity at different co-polarization and cross-polarization ratios, a coefficient of agreement analysis was carried out for nominal scales (kappa), and a global accuracy matrix using field data on plot burn severity (CBI) [1,5,12,44,51,53]. Cross-ratios of absolute and relative cross-polarization values VH_2 ($k = 0.734$) and the RBR by RDFI ($k = 0.799$) were shown to be the most reliable for determining burn severity, showing consistent overall accuracy and considerable strength of agreement [1,5,12,44,51,53]. The behavior of the CBI in the field proposed by Key and Benson [49], adapted and modified for this study, was significant (Table 4), and adequate responses to VV and VH polarizations were obtained (Figures 2–4). We obtained a significant response to the VV and VH polarization (Figures 2–4) because the CBI field protocol takes into account the sensor orientation (downward), improving the canopy and understory attenuation layer consumption and the indirect estimates due to the effect of soil exposure, and generating a high relative measurement in the detection of burn severity by the sensor (Figures 2–4) [17–19,39,52,54,55,67].

Our results show a scientific basis for the use of active imagery such as C-band SAR Sentinel-1 in the detection and quantification of burn severity in the Peruvian Amazon. The results give VH cross-polarization using absolute/relative ratio and RDFI as the best predictors. Future research should focus on further validating the behavior of burn severity in different forest types in the Amazon region and generating monitoring methods on a large scale. Likewise, the fusion of global optical images such as Sentinel-2 and Landsat with SAR images should be studied to evaluate detection and accuracy versus independent analysis of optical or SAR images.

5. Conclusions

The research provides knowledge about the use of 2020 Sentinel-1 C-band SAR imagery in the estimation of burn severity in the southeastern Peruvian Amazon. We applied absolute, relative, and Burn Ratio (RBR) predictors by means of the Radar Forest Degradation Index (RDFI) and verified the accuracy with field data on plot fire severity (CBI).

The use of simple cross-polarization (VH) determined the absolute/relative predictor (1. Ab_Rel_VH_2 = 3972 ha) and RDFI (2. VVVH = 3496 ha) with the best dispersion responses, with accuracies of a kappa index (k) of 0.734 (1) and 0.799 (2). The highest occurrences and incidences were recorded at the moderate (43%) and high (40%) levels.

According to our analysis, the behavior of the co-polarization (VV) and cross-polarization (VH) of the C-band SAR Sentinel-1 varied according to the terrain physiography and vegetation physiognomy. The backscattering of VH allowed for better detection at surface and depth, while the co-polarization (VV) was more affected by scattering processes and demonstrated a strong relationship of burning severity in a stable and dry environment that matched the burning seasonality in the Amazon. On the other hand, the limitations of using co-polarization backscattering and cross-polarization were minimized by the application of RDFI, which uses VV and VH polarizations pre- and post-burning. In our case, the results were as expected according to the theoretical basis of radar image backscattering. However, we suggest further analysis for other reductions.

Supplementary Materials: The following supporting information can be downloaded at: <https://www.mdpi.com/article/10.3390/fire5040094/s1>, Figure S1: Distribution of samples to validate the severity of burns in the district of Tahuamanu, southeastern Peruvian Amazon; Figure S2: Sentinel-1 C-band SAR images with VV polarization pre- and post-fire 2020; Figure S3: Sentinel-1 C-band SAR images with VH polarization pre- and post-fire 2020; Figure S4: Determination of burned areas using absolute and relative values of pre- and post-fire 2020 VV_1 backscatter data; Equations (1) and (3); Figure S5: Determination of burned areas using absolute and relative values of pre- and post-fire

2020 VV_2 backscatter data; Equations (1) and (5); Figure S6: Determination of burned areas using absolute and relative values of pre- and post-fire 2020 VH_1 backscatter data; Equations (2) and (4); Figure S7: Determination of burned areas using absolute and relative values of pre- and post-fire 2020 VH_2 backscatter data; Equations (2) and (6); Figure S8: Determination of burned areas through Burn Ratio (RBR) by Radar Forest Degradation Index (RDFI) from pre- and post-fire 2020 VV and VH backscatter data; Equations (8) and (9); Figure S9: Burn severity using absolute, relative values from VV_1 pre- and post-fire 2020 backscatter data; Equations (1) and (3); Figure S10: Burn severity using absolute, relative values from VV_2 pre- and post-fire 2020 backscatter data; Equations (1) and (5); Figure S11: Burn severity using absolute, relative values from VH_1 pre- and post-fire 2020 backscatter data; Equations (2) and (4); Figure S12: Burn severity using absolute, relative values from VH_2 pre- and post-fire 2020 backscatter data; Equations (2) and (6); Figure S13: Burn severity using Radar Burn Ratio (RBR) and Radar Forest Degradation Index (RDFI) of pre- and post-fire 2020 VV and VH backscatter data; Equations (7)–(9); Table S1: Sentinel-1 image acquisition information; Table S2: Sentinel-1 satellite image characteristics.

Author Contributions: Conceptualization, G.A.-A. and R.F.M.F.; methodology, G.A.-A. and R.F.M.F.; software, R.F.M.F., G.A.-A., R.C.-R., D.R.E. and J.G.-Q.; validation, R.F.M.F., G.A.-A. and J.G.-Q.; formal analysis, R.F.M.F., G.A.-A., D.R.E. and J.G.-Q.; research, R.F.M.F., G.A.-A., D.R.E. and J.G.-Q.; data curation, R.F.M.F. and G.A.-A.; writing—original draft, R.F.M.F.; writing—revising and editing, G.A.-A., L.R.-A., J.G.-Q. and D.R.E.; visualization, G.A.-A., L.R.-A. and J.G.-Q.; project administration, G.A.-A.; fund raising, G.A.-A. All authors have read and agreed to the published version of the manuscript.

Funding: This research received no external funding.

Data Availability Statement: Not applicable.

Conflicts of Interest: The authors declare no conflict of interest.

References

1. Cannon, S.H.; Gartner, J.E.; Rupert, M.G.; Michael, J.A.; Rea, A.H.; Parrett, C. Predicting the probability and volume of postwildfire debris flows in the intermountain western United States. *Bulletin* **2010**, *122*, 127–144. [\[CrossRef\]](#)
2. Cannon, S.H.; DeGraff, J. The increasing wildfire and post-fire debris-flow threat in western USA, and implications for consequences of climate change. In *Landslides—Disaster Risk Reduction*; Springer: Berlin/Heidelberg, Germany, 2009; pp. 177–190. [\[CrossRef\]](#)
3. Addison, P.; Oommen, T. Utilizing satellite radar remote sensing for burn severity estimation. *Int. J. Appl. Earth Obs. Geoinf.* **2018**, *73*, 292–299. [\[CrossRef\]](#)
4. Kern, A.N.; Addison, P.; Oommen, T.; Salazar, S.E.; Coffman, R.A. Machine learning based predictive modeling of debris flow probability following wildfire in the intermountain Western United States. *Math. Geosci.* **2017**, *49*, 717–735. [\[CrossRef\]](#)
5. Parks, S.A.; Dillon, G.K.; Miller, C. A new metric for quantifying burn severity: The relativized burn ratio. *Remote Sens.* **2014**, *6*, 1827–1844. [\[CrossRef\]](#)
6. Brown, A.R.; Petropoulos, G.P.; Ferentinis, K.P. Appraisal of the Sentinel-1 & 2 use in a large-scale wildfire assessment: A case study from Portugal's fires of 2017. *Appl. Geogr.* **2018**, *100*, 78–89. [\[CrossRef\]](#)
7. Colson, D.; Petropoulos, G.P.; Ferentinis, K.P. Exploring the Potential of Sentinels-1 & 2 of the Copernicus Mission in Support of Rapid and Cost-effective Wildfire Assessment. *Int. J. Appl. Earth Obs. Geoinf.* **2018**, *73*, 262–276. [\[CrossRef\]](#)
8. Belenguer-Plomer, M.A.; Tanase, M.A.; Chuvieco, E.; Bovolo, F. CNN-based burned area mapping using radar and optical data. *Remote Sens. Environ.* **2021**, *260*, 112468. [\[CrossRef\]](#)
9. Stroppiana, D.; Azar, R.; Calò, F.; Pepe, A.; Imperatore, P.; Boschetti, M.; Silva, J.; Brivio, P.A.; Lanari, R. Integration of optical and SAR data for burned area mapping in Mediterranean Regions. *Remote Sens.* **2015**, *7*, 1320–1345. [\[CrossRef\]](#)
10. Allison, R.S.; Johnston, J.M.; Craig, G.; Jennings, S. Airborne optical and thermal remote sensing for wildfire detection and monitoring. *Sensors* **2016**, *16*, 1310. [\[CrossRef\]](#)
11. Meng, R.; Wu, J.; Zhao, F.; Cook, B.D.; Hanavan, R.P.; Serbin, S.P. Measuring short-term post-fire forest recovery across a burn severity gradient in a mixed pine-oak forest using multi-sensor remote sensing techniques. *Remote Sens. Environ.* **2018**, *210*, 282–296. [\[CrossRef\]](#)
12. Murphy, K.A.; Reynolds, J.H.; Koltun, J.M. Evaluating the ability of the differenced Normalized Burn Ratio (dNBR) to predict ecologically significant burn severity in Alaskan boreal forests. *Int. J. Wildland Fire* **2008**, *17*, 490–499. [\[CrossRef\]](#)
13. Lertsakdadet, B.S.; Kennedy, G.T.; Stone, R.; Kowalczewski, C.; Kowalczewski, A.C.; Natesan, S.; Christy, R.J.; Durkin, A.J.; Choi, B. Assessing multimodal optical imaging of perfusion in burn wounds. *Burns* **2021**, *48*, 799–807. [\[CrossRef\]](#)
14. Gibson, L.; Engelbrecht, J.; Rush, D. Detecting historic informal settlement fires with Sentinel 1 and 2 satellite data—Two case studies in Cape Town. *Fire Saf. J.* **2019**, *108*, 102828. [\[CrossRef\]](#)

15. Zhang, Q.; Ge, L.; Zhang, R.; Metternicht, G.I.; Du, Z.; Kuang, J.; Xu, M. Deep-learning-based burned area mapping using the synergy of Sentinel-1 & 2 data. *Remote Sens. Environ.* **2021**, *264*, 112575. [\[CrossRef\]](#)
16. Chuvieco, E.; Mouillot, F.; van der Werf, G.R.; San Miguel, J.; Tanase, M.; Koutsias, N.; García, M.; Yebra, M.; Padilla, M.; Gitas, I.; et al. Historical background and current developments for mapping burned area from satellite Earth observation. *Remote Sens. Environ.* **2019**, *225*, 45–64. [\[CrossRef\]](#)
17. Tanase, M.A.; Kennedy, R.; Aponte, C. Fire severity estimation from space: A comparison of active and passive sensors and their synergy for different forest types. *Int. J. Wildland Fire* **2015**, *24*, 1062–1075. [\[CrossRef\]](#)
18. Tanase, M.A.; Kennedy, R.; Aponte, C. Radar Burn Ratio for fire severity estimation at canopy level: An example for temperate forests. *Remote Sens. Environ.* **2015**, *170*, 14–31. [\[CrossRef\]](#)
19. Viedma, O.; Chico, F.; Fernández, J.J.; Madrigal, C.; Safford, H.D.; Moreno, J.M. Disentangling the role of prefire vegetation vs. burning conditions on fire severity in a large forest fire in SE Spain. *Remote Sens. Environ.* **2020**, *247*, 111891. [\[CrossRef\]](#)
20. Dos Reis, M.; Graça, P.M.L.d.A.; Yanai, A.M.; Ramos, C.J.P.; Fearnside, P.M. Forest fires and deforestation in the central Amazon: Effects of landscape and climate on spatial and temporal dynamics. *J. Environ. Manag.* **2021**, *288*, 112310. [\[CrossRef\]](#)
21. Melo, V.F.; Barros, L.S.; Silva, M.C.S.; Veloso, T.G.R.; Senwo, Z.N.; Matos, K.S.; Nunes, T.K.O. Soil bacterial diversities and response to deforestation, land use and burning in North Amazon, Brazil. *Appl. Soil Ecol.* **2021**, *158*, 103775. [\[CrossRef\]](#)
22. Santos, A.M.d.; Silva, C.F.A.d.; Rudke, A.P.; Oliveira Soares, D.d. Dynamics of active fire data and their relationship with fires in the areas of regularized indigenous lands in the Southern Amazon. *Remote Sens. Appl. Soc. Environ.* **2021**, *23*, 100570. [\[CrossRef\]](#)
23. Kasischke, E.S.; Melack, J.M.; Dobson, M.C. The use of imaging radars for ecological applications—A review. *Remote Sens. Environ.* **1997**, *59*, 141–156. [\[CrossRef\]](#)
24. Collins, L.; Bennett, A.F.; Leonard, S.W.J.; Penman, T.D. Wildfire refugia in forests: Severe fire weather and drought mute the influence of topography and fuel age. *Glob. Chang. Biol.* **2019**, *25*, 3829–3843. [\[CrossRef\]](#)
25. Sánchez, M.E.G.; Borja, M.E.L.; Álvarez, P.A.P.; Romero, J.G.; Cozar, J.S.; Navarro, D.M.; de las Heras Ibáñez, J. Efecto de los trabajos de restauración forestal post-incendio en ladera sobre la recuperación de la funcionalidad del suelo. *Cuad. De La Soc. Española De Cienc. For.* **2019**, *45*, 35–44.
26. Dourojeanni, M. Esbozo de una nueva política forestal peruana. *Rev. For. Del Perú* **2019**, *34*, 4–20. [\[CrossRef\]](#)
27. Perz, S.; Qiu, Y.; Xia, Y.; Southworth, J.; Sun, J.; Marsik, M.; Rocha, K.; Passos, V.; Rojas, D.; Alarcón, G.; et al. Trans-boundary infrastructure and land cover change: Highway paving and community-level deforestation in a tri-national frontier in the Amazon. *Land Use Policy* **2013**, *34*, 27–41. [\[CrossRef\]](#)
28. Chávez, A.; Huamani, L.; Fernandez, R.; Bejar, N.; Valera, F.; Perz, S.; Brown, I.; Domínguez, S.; Pinedo, R.; Alarcón, G. Regional Deforestation Trends within Local Realities: Land-Cover Change in Southeastern Peru 1996–2011. *Land* **2013**, *2*, 131–157. [\[CrossRef\]](#)
29. Alarcón, G.; Díaz, J.; Vela, M.; García, M.; Gutiérrez, J. Deforestación en el sureste de la amazonia del Perú entre los años 1999–2013; caso Regional de Madre de Dios (Puerto Maldonado–Inambari). *J. High Andean Res.* **2016**, *18*, 319–330. [\[CrossRef\]](#)
30. Perz, S.; Castro, W.; Rojas, R.; Castillo, J.; Chávez, A.; García, M.; Guadalupe, Ó.; Gutiérrez, T.; Hurtado, A.; Mamani, Z.; et al. La Amazonia como un sistema socio-ecológico: Las dinámicas de cambios complejos humanos y ambientales en una frontera trinacional. In *Naturaleza y Sociedad: Perspectivas Socio-Ecológicas Sobre Cambios Globales en América Latina*; Postigo, J., Young, K., Eds.; Desco, IEP e INTE-PUCP: Lima, Perú, 2016; p. 444.
31. GOREMAD; IIAP. *Macro Zonificación Ecológica Económica de Madre de Dios*; Gobierno Regional de Madre de Dios: Puerto Maldonado, Peru, 2009; p. 208.
32. Román-Dañobeytia, F.; Cabanillas, F.; Lefebvre, D.; Farfan, J.; Alferez, J.; Polo-Villanueva, F.; Llacsahuanga, J.; Vega, C.M.; Velasquez, M.; Corvera, R.; et al. Survival and early growth of 51 tropical tree species in areas degraded by artisanal gold mining in the Peruvian Amazon. *Ecol. Eng.* **2021**, *159*, 106097. [\[CrossRef\]](#)
33. Román-Dañobeytia, F.; Huayllani, M.; Michi, A.; Ibarra, F.; Loayza-Muro, R.; Vázquez, T.; Rodríguez, L.; García, M. Reforestation with four native tree species after abandoned gold mining in the Peruvian Amazon. *Ecol. Eng.* **2015**, *85*, 39–46. [\[CrossRef\]](#)
34. Holdridge, L.R. Life zone ecology. In *Life Zone Ecology*; Springer: Berlin/Heidelberg, Germany, 1967.
35. SENAMHI. *Mapa de Clasificación Climática del Perú*; Servicio Nacional de Meteorología e Hidrología del Perú: Lima, Perú, 2012.
36. SENAMHI. *En la Selva Preparémonos para la Llegada de los Friaies*; Servicio Nacional de Meteorología e Hidrología del Perú: Lima, Perú, 2015.
37. Escobar, A.A.H.; Rodríguez, M.P.R.; López, B.M.P.; Ganchozo, B.I.; Gómez, A.J.Q.; Ponce, L.A.M. *Metodología de la Investigación Científica*; 3Ciencias: Alcoy, Spain, 2018; Volume 15.
38. Bernhard, E.-M.; Twele, A.; Gähler, M. Rapid mapping of forest fires in the European Mediterranean region—A change detection approach using X-band SAR-data. *Photogramm.-Fernerkund.-Geoinf.* **2011**, *2011*, 261–270. [\[CrossRef\]](#)
39. Tanase, M.A.; Santoro, M.; Aponte, C.; de la Riva, J. Polarimetric properties of burned forest areas at C-and L-band. *IEEE J. Sel. Top. Appl. Earth Obs. Remote Sens.* **2013**, *7*, 267–276. [\[CrossRef\]](#)
40. Xiuwan, C. Using remote sensing and GIS to analyse land cover change and its impacts on regional sustainable development. *Int. J. Remote Sens.* **2002**, *23*, 107–124. [\[CrossRef\]](#)
41. Jensen, J.R.; Lin, H.; Yang, X.; Ramsey III, E.; Davis, B.A.; Thoenke, C.W. The measurement of mangrove characteristics in southwest Florida using SPOT multispectral data. *Geocarto Int.* **1991**, *6*, 13–21. [\[CrossRef\]](#)

42. Anaya, J.A.; Chuvieco, E. Validación para Colombia de la estimación de área quemada del producto L3JRC en el periodo 2001–2007/Validation of the L3JRC burned area product estimation in Colombia from 2001 to 2007. *Actual. Biológicas* **2010**, *32*, 29.
43. Chuvieco, E.; Hantson, S. Procesamiento Estándar de Imágenes Landsat. Documento Técnico de Algoritmos a Aplicar. Version 1. Plan Nacional de Teledetección. Instituto Geográfico Nacional. En Línea. 2010. Available online: http://www.ign.es/PNT/pdf/especificacionestecnicas-pnt-mediari-landsat_v2-2010.pdf (accessed on 31 January 2022).
44. Ochoa, C.; Páez, O. Inferencia estadística: Probabilidad, variables aleatorias y distribuciones de probabilidad. *Evid. Pediatr.* **2019**, *15*, 27.
45. Elijah, R.; Jensen, J.R. Remote Sensing of Mangrove Wetlands: Relating Canopy Spectra to Site-Specific Data. 1996. Available online: https://www.asprs.org/wp-content/uploads/pers/1996journal/aug/1996_aug_939-948.pdf (accessed on 31 January 2022).
46. Chuvieco, E. *Teledetección Espacial: La Observación de la Tierra Desde el Espacio*; Digital Reasons: Barcelona, Spain, 2002.
47. Kuhn, M.; Johnson, K. *Applied Predictive Modeling*; Springer: Berlin/Heidelberg, Germany, 2013; Volume 26.
48. Townsend, J.T. Theoretical analysis of an alphabetic confusion matrix. *Percept. Psychophys.* **1971**, *9*, 40–50. [[CrossRef](#)]
49. Key, C.H.; Benson, N.C. Landscape Assessment (LA). In *FIREMON: Fire Effects Monitoring and Inventory System*; General Technical Report RMRS-GTR-164-CD; Lutes, D.C., Keane, R.E., Caratti, J.F., Key, C.H., Benson, N.C., Sutherland, S., Gangi, L.J., Eds.; US Department of Agriculture, Forest Service, Rocky Mountain Research Station: Fort Collins, CO, USA, 2006; Volume 164, p. LA-1-55. Available online: https://www.fs.fed.us/rm/pubs/rmrs_gtr164/rmrs_gtr164_13_land_assess.pdf (accessed on 31 January 2022).
50. Cerda, J.; Villarroel, L. Evaluación de la concordancia inter-observador en investigación pediátrica: Coeficiente de Kappa. *Rev. Chil. De Pediatría* **2008**, *79*, 54–58. [[CrossRef](#)]
51. Cohen, J. A Coefficient of Agreement for Nominal Scales. *Educ. Psychol. Meas.* **1960**, *20*, 37–46. [[CrossRef](#)]
52. Li, X.; Zhou, Y.; Gong, P.; Seto, K.C.; Clinton, N. Developing a method to estimate building height from Sentinel-1 data. *Remote Sens. Environ.* **2020**, *240*, 111705. [[CrossRef](#)]
53. Cruz, M.G.; Alexander, M.E. Uncertainty associated with model predictions of surface and crown fire rates of spread. *Environ. Model. Softw.* **2013**, *47*, 16–28. [[CrossRef](#)]
54. Tanase, M.A.; Santoro, M.; de La Riva, J.; Fernando, P.; Le Toan, T. Sensitivity of X-, C-, and L-band SAR backscatter to burn severity in Mediterranean pine forests. *IEEE Trans. Geosci. Remote Sens.* **2010**, *48*, 3663–3675. [[CrossRef](#)]
55. Tanase, M.A.; Santoro, M.; Wegmüller, U.; de la Riva, J.; Pérez-Cabello, F. Properties of X-, C-and L-band repeat-pass interferometric SAR coherence in Mediterranean pine forests affected by fires. *Remote Sens. Environ.* **2010**, *114*, 2182–2194. [[CrossRef](#)]
56. Torres, R.; Snoei, P.; Geudtner, D.; Bibby, D.; Davidson, M.; Attema, E.; Potin, P.; Rommen, B.; Floury, N.; Brown, M. GMES Sentinel-1 mission. *Remote Sens. Environ.* **2012**, *120*, 9–24. [[CrossRef](#)]
57. Alarcon, G.; Canahuire, R.R.; Guevarra, F.M.G.; Rodriguez, L.; Gallegos, L.E.; Garate-Quispe, J. Dinámica de la pérdida de bosques en el sureste de la Amazonia peruana: Un estudio de caso en Madre de Dios. *Ecosistemas* **2021**, *30*, 2175. [[CrossRef](#)]
58. Chavez, A.B.; Perz, S.G. Path dependency and contingent causation in policy adoption and land use plans: The case of Southeastern Peru. *Geoforum* **2013**, *50*, 138–148. [[CrossRef](#)]
59. Chavez, A.; Huamani, L.; Vilchez, H.; Perz, S.; Quaedvlieg, J.; Rojas, R.; Brown, F.; Pinedo, R. The effects of climate change variability on rural livelihoods in Madre de Dios, Peru. *Reg. Environ. Chang.* **2020**, *20*, 70. [[CrossRef](#)]
60. Coen, J.L.; Stavros, E.N.; Fites-Kaufman, J.A. Deconstructing the King megafire. *Ecol. Appl.* **2018**, *28*, 1565–1580. [[CrossRef](#)]
61. De Oliveira Alves, N.; de Souza Hacon, S.; de Oliveira Galvão, M.F.; Simões Peixotoc, M.; Artaxo, P.; de Castro Vasconcellos, P.; de Medeiros, S.R.B. Genetic damage of organic matter in the Brazilian Amazon: A comparative study between intense and moderate biomass burning. *Environ. Res.* **2014**, *130*, 51–58. [[CrossRef](#)]
62. De Oliveira Alves, N.; Brito, J.; Caumo, S.; Arana, A.; de Souza Hacon, S.; Artaxo, P.; Hillamo, R.; Teinilä, K.; Batistuzzo de Medeiros, S.R.; de Castro Vasconcellos, P. Biomass burning in the Amazon region: Aerosol source apportionment and associated health risk assessment. *Atmos. Environ.* **2015**, *120*, 277–285. [[CrossRef](#)]
63. Porcher, V.; Thomas, E.; Gomringer, R.C.; Lozano, R.B. Fire- and distance-dependent recruitment of the Brazil nut in the Peruvian Amazon. *For. Ecol. Manag.* **2018**, *427*, 52–59. [[CrossRef](#)]
64. Smith, J.; van de Kop, P.; Reategui, K.; Lombardi, I.; Sabogal, C.; Diaz, A. Dynamics of secondary forests in slash-and-burn farming: Interactions among land use types in the Peruvian Amazon. *Agric. Ecosyst. Environ.* **1999**, *76*, 85–98. [[CrossRef](#)]
65. Morello, T.; Anderson, L.; Silva, S. Innovative fire policy in the Amazon: A statistical Hicks-Kaldor analysis. *Ecol. Econ.* **2022**, *191*, 107248. [[CrossRef](#)]
66. Leite-Filho, A.T.; Costa, M.H.; Fu, R. The southern Amazon rainy season: The role of deforestation and its interactions with large-scale mechanisms. *Int. J. Climatol.* **2020**, *40*, 2328–2341. [[CrossRef](#)]
67. Stevens, L.E.; Schenk, E.R.; Springer, A.E. Springs ecosystem classification. *Ecol. Appl.* **2020**, *31*, e2218. [[CrossRef](#)]
68. Southworth, J.; Marsik, M.; Qiu, Y.; Perz, S.; Cumming, G.; Stevens, F.; Rocha, K.; Duchelle, A.; Barnes, G. Roads as Drivers of Change: Trajectories across the Tri-National Frontier in MAP, the Southwestern Amazon. *Remote Sens.* **2011**, *3*, 1047–1066. [[CrossRef](#)]
69. Belenguer-Plomer, M.A.; Tanase, M.A.; Fernandez-Carrillo, A.; Chuvieco, E. Burned area detection and mapping using Sentinel-1 backscatter coefficient and thermal anomalies. *Remote Sens. Environ.* **2019**, *233*, 111345. [[CrossRef](#)]
70. Bradstock, R.A.; Hammill, K.A.; Collins, L.; Price, O. Effects of weather, fuel and terrain on fire severity in topographically diverse landscapes of south-eastern Australia. *Landsc. Ecol.* **2010**, *25*, 607–619. [[CrossRef](#)]

71. Hernández, H.M. Lo que Usted Debe Saber Sobre Incendios de Cobertura Vegetal. 2019. Available online: https://repositorio.gestiondelriesgo.gov.co/bitstream/handle/20.500.11762/28309/Cartilla_Incendios_2019-.pdf?sequence=4 (accessed on 31 January 2022).
72. Lahaye, S.; Curt, T.; Fréjaville, T.; Sharples, J.; Paradis, L.; Hély, C. What are the drivers of dangerous fires in Mediterranean France? *Int. J. Wildland Fire* **2018**, *27*, 155–163. [[CrossRef](#)]
73. Martins, F.d.S.R.V.; dos Santos, J.R.; Galvão, L.S.; Xaud, H.A.M. Sensitivity of ALOS/PALSAR imagery to forest degradation by fire in northern Amazon. *Int. J. Appl. Earth Obs. Geoinf.* **2016**, *49*, 163–174. [[CrossRef](#)]